Measurement-based Analysis of Specular- and Dense Multipath Components at 94 GHz in an Indoor Environment

Brecht Hanssens, María-Teresa Martínez-Inglés, Emmeric Tanghe, David Plets, José-María Molina-García-Pardo, Claude Oestges, Luc Martens, and Wout Joseph

***Abstract*—In this paper, we present a measurement-based analysis of the indoor radio channel characteristics of both the specular and dense multipath components (SMC and DMC) at 94 GHz within a 3 GHz bandwidth. Based on an investigation of the frequency-stationarity of this band, we have selected multiple sub-bands to perform our evaluation. A method is developed that allowed for the estimation of the specular propagation paths, after which the remainder is regarded as the diffuse spectrum. Radio channel characteristics such as the path loss, root-mean-square delay spread and the SMC ratio have been calculated as a function of transmitter-receiver distance, and in the different sub-bands. Based on the diffuse spectrum, the behavior of the reverberation time is analyzed for the first time in the 94 GHz band.**

I. Introduction

Over recent years, the W-band of the electromagnetic spectrum, ranging from 75 GHz to 110 GHz, has received considerable attention with the continuously expanding demand for higher data rates. The increasing amount of mobile devices in this modern age necessitates the optimal use of the vacant parts in the available spectrum, especially those which employ a wide frequency range. Since the lower frequency bands below 6 GHz are becoming heavily-utilized, new and unused frequency bands are being investigated. The W-band offers a license-free part of the spectrum to overcome these issues. The W-band is primarily used for satellite communications, millimeter-wave radar, and tracking applications for body-centric and short-range distances.

In 2003, the Federal Communications Commission (FCC) ruled that the frequency spectrum from 92 GHz to 95 GHz was to be made available for high-density fixed wireless services, boosting scientific research around this topic. A beneficial aspect about this high frequency, which makes it interesting for millimeter-wave body-centric systems, is the ability of the electromagnetic waves to penetrate optically opaque materials, such as dust, fog and clothing, and reflect off skin [1]. This makes millimeter-wave imaging systems at this frequency ideal for security scanners, collision avoidance systems [2], and localization frameworks. Presently, only very few studies aim to investigate the indoor propagation characteristics of this frequency band, of which the first narrow- and wideband results can be found in [3] and [4], respectively. In [5], wideband measurement results are presented over the entire W-band, but are limited to a distance of less than 0.5 m. Therefore, this work aims to overcome these gaps in the literature by presenting wideband propagation characteristics of the 94 GHz band in an indoor environment, with distances between transmitter and receiver up to 6 m.

The novelty of this work is that we have performed the first wideband analysis of the specular and dense multipath components (SMC and DMC) of this frequency band ever. It is based on the method described in [6], but applied for the processing of wideband measurement data in the 94 GHz band. Furthermore, by estimating the diffuse spectrum from the measurement data, we are able to present the behavior of the reverberation time at 94 GHz, known from the theory of room electromagnetics (RE) [7]. This theory states that there is an exponential decay of the electromagnetic field in a room, under the assumption of rich scattering, and that the energy density is constant across the entire room. The reverberation time (i.e., the time for the electromagnetic waves to uniformly distribute themselves in a room) depends only on the volume of the room, its surface area and an effective absorption coefficient, and is assumed to be constant across this room. Such an approach easily allows to characterize the radio channel on a room-to-room basis. The RE theory has never been evaluated for this frequency band up to now, so we will analyze whether it is valid in the considered environment.

This paper is the extended work of [8], [9], which only analyzes the 94 GHz band in its entirety. The structure of this paper is as follows: Section II describes the measurement scenario and the channel sounding procedure. Section III covers the evaluation of the obtained measurement data, and describes how the results in Section IV of our analysis are obtained. Ultimately, Section V summarizes this paper with the conclusions and some ideas for future work.

II. Measurements

A. Measurement environment

The channel sounding measurements were carried out in a laboratory of the Technical University of Cartagena, Spain. In

M.T. Martínez-Inglés is with the University Center of Defense, San Javier Air Force Base, Ministerio de Defensa-Universidad Politécnica de Cartagena, Cartagena, Spain.

J.-M. Molina-García-Pardo is with the Information Technologies and Communications Department, Universidad Politécnica de Cartagena, Cartagena, Spain.

C. Oestges is with ICTEAM, Université catholique de Louvain, Louvain-la-Neuve, Belgium.

B. Hanssens, E. Tanghe, D. Plets, L. Martens and W. Joseph are with INTEC-WAVES, Ghent University / imec, Ghent, Belgium. Email address of the corresponding author: Brecht.Hanssens@UGent.be

Fig. 1, the measurement scenario is depicted, in which one fixed position acts as the receiver (marked as ULA_{1x5}), whilst the transmitter occupies various positions across this room (for a total of 15 uniformly distributed positions, marked 1 to 15).

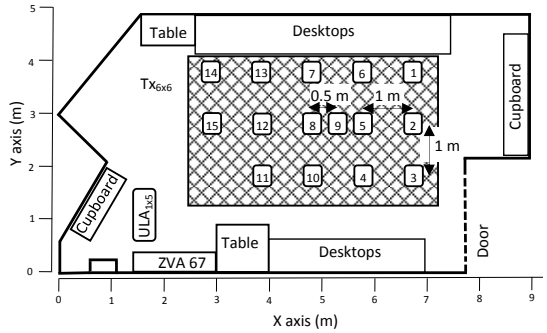

(a) Measurement scenario and -environment

(b) Photo 1: center of the room, looking towards the left in Fig. 1a

(c) Photo 1: center of the room, looking towards the right in Fig. 1a

Figure 1: Representation of the measurement scenario and -environment.

Fig. 1b and 1c show the laboratory in two panoramic photos, each showing one side of the room. The laboratory size is approximately 8×4.8×3.5 meters (see also Fig. 1a), and it is furnished with several cupboards, chairs, and tables on which numerous computers and electronic devices stand. The walls are typical interior walls, made of plasterboard, whilst the floor and ceiling are made of concrete.

B. Channel sounding procedure

In order to obtain the channel transfer function, a Vector Network Analyzer (VNA) of type Rohde & Schwarz (R&S) ZVA67 was used to measure the complex radio channel gain in the indoor millimeter-wave (mmW) channel ranging from 92.5 GHz up to 95.5 GHz, representing the so called 94 GHz band. Since the absolute bandwidth exceeds 500 MHz, this is considered to be a wideband scenario according to the FCC [10]. Both at the transmitter (Tx) and the receiver (Rx), vertically polarized omni-directional antennas were used, manufactured by Mi-Wave (WR-10). They operate at a center frequency of 94 GHz with a 3 GHz bandwidth and a typical nominal VSWR of 1.5:1. They feature 2 dB gain and 30° beamwidth in the elevation plane, having omni-directionality in the horizontal plane. The antenna pattern measured from 0 to 350° with a step of 10° resulted in a difference of at minimum -1.2 dBc and maximum +1.6 dBc (relative level of noise or sideband power compared with the carrier power). The Tx was mounted at a height of 0.89 m, whilst the Rx was mounted at a height of 0.78 m. The configuration of the VNA is summarized in Table I. The near field (Fraunhofer) distance for the considered scenario (specific antenna and frequency band considered) was found to be 3.9785 mm. Further information about this channel sounding procedure can be found in [11].

Table I: Settings of the VNA channel sounding procedure.

Parameter	Value
Center frequency	94 GHz
Frequency band	92.5 GHz - 95.5 GHz
Intermediate frequency	10 Hz
Number of frequency points	1024
Frequency separation	2.932 MHz

At both ends of the measurement system, a virtual antenna array was created by an automated positioning system on which the antennas were mounted, using Arricks Robotics positioners. This virtual Multiple-Input Multiple-Output (MIMO) measurement system consists of a Uniform Rectangular Array (URA) at Tx and a Uniform Linear Array (ULA) at Rx. For the URA at Tx, the antenna was moved over a 6×6 uniform rectangular grid with 1.4 mm spacing (corresponding with 0.44 λ at 94 GHz) along the x- and y-axis. For the ULA at Rx, 5 elements were equally spaced with 1 mm spacing (corresponding with 0.31 λ at 94 GHz) along the y-axis. The VNA then measured the complex gain between each combination of transmit- and receive antennas in the virtual array, thus measuring the VV-polarized radio channel. By sampling the 94 GHz band over $M_f = 1024$ uniformly spaced frequency points between 92.5 GHz and 95.5 GHz, we were able to obtain a maximum measurable time-delay τ_{max} of 341 ns with a time-delay bin width $\Delta\tau$ of 0.33 ns.

In our measurement setup, we obtained a dynamic range (i.e., the difference between the maximum- and minimum signal strength) of 45 dB for the closest measurement positions at 1.5 m, and 35 dB for the ones further away at 5.5 m. All frequency-swept measurements with virtual arrays were carried out in static radio channel conditions.

III. Evaluation

A. Frequency stationarity

Prior to the processing of the measurement data in the 3 GHz band at 94 GHz, we will first check the uncorrelated scattering (US) assumption which is often assumed for the modeling of wireless channels. The US assumption states that the second order statistical description of the radio channel is independent of the absolute frequency, which implies that channel contributions at different time-delays are uncorrelated. In order to evaluate the US assumption in the aforementioned 3 GHz band at 94 GHz, we will apply the procedure explained in detail in [12], relying on the use of the collinearity metric. This metric measures the overlap in signal space between two

power spectral densities, and enables a US test to define a frequency stationarity region (or stationarity bandwidth) in which the collinearity exceeds a certain threshold. We analyze the stationarity bandwidths for the different measurement positions (sorted by Tx-Rx distance) as a function of the applied threshold values, for a minimum stationarity region (MSR) of 375 MHz (corresponding with 128 frequency samples) in which the US property locally holds. Choosing a smaller value for the MSR would deteriorate its resolution.

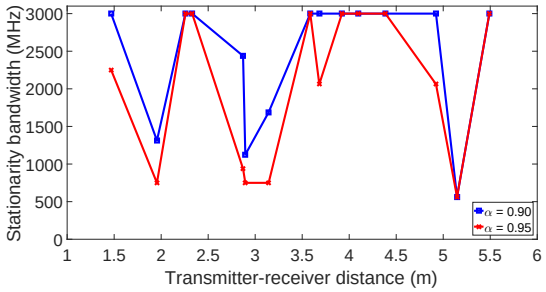

Figure 2: Stationarity bandwidth as a function of Tx-Rx distance.

Fig. 2 shows that with a strong criterion of 0.95 [12] for the collinearity threshold, certain measurement positions only have a stationarity bandwidth of about 500 to 750 MHz, whilst for other measurement positions, the US assumption holds for the entire 3 GHz band. Taking these results into account, we choose to analyze the 3 GHz band as a whole ([92.50-95.50 GHz]), and compare it to the analysis of dividing this band into four sub-bands of 750 MHz. In each sub-band, we have 256 frequency samples, reducing the time-delay bin width from $\Delta\tau|_{total} = 0.33$ ns to $\Delta\tau|_{sub} = 1.33$ ns, whilst the maximum time-delay $\tau|_{max}$ stays 341 ns. We will use the following abbreviations to refer to each frequency band:

total band:	**92.50 – 95.50 GHz**
sub-band A:	92.50 – 93.25 GHz
sub-band B:	93.25 – 94.00 GHz
sub-band C:	94.00 – 94.75 GHz
sub-band D:	94.75 – 95.50 GHz

B. Power delay profiles

This subsection describes how an Average Power Delay Profile (APDP) is calculated from the measurement data obtained from our channel sounding procedure. The subsequent calculation focuses on the entire 3 GHz band with $M_{f,total} = 1024$ frequency samples, but it is straightforward to extend it to calculate an APDP in each sub-band with $M_{f,sub} = 256$ samples. We first calculate the channel impulse response $h^m(n)$ for the m^{th} Tx-Rx antenna pair as follows:

$$h^m(n) = \frac{1}{\sqrt{Mf}} \sum_{k=1}^{M_f} w_k H_k^m \exp\left(j2\pi n \tfrac{k-1}{Mf}\right), \qquad (1)$$

in which H_k^m is the channel frequency response in the k^{th} frequency bin for the m^{th} antenna pair, and is first multiplied with the k^{th} bin of the window function w. In this work, we have used a Hann window function for its good trade-off between a wider main lobe and reduced side lobe levels. The discrete variable n denotes the n^{th} delay bin in the time-delay domain. Note that Eq. (1) corresponds to an inverse discrete Fourier transform (IDFT) operation on the original signal. The Power Delay Profile (PDP) $P^m(n)$ can then be calculated from $h^m(n)$ as follows:

$$P^m(n) = |h^m(n)|^2. \qquad (2)$$

Each of the $M_{TR} = M_T \times M_R$ separate PDPs for every combination of Tx- and Rx antennas at a single measurement position are subsequently averaged to construct an APDP, in order to remove the effect of small-scale fading. The APDP for the total channel between transmitter and receiver at this measurement position can then be written as follows:

$$P_{Meas}(n) = \frac{1}{M_{TR}} \sum_{m=1}^{M_{TR}} P^m(n). \qquad (3)$$

Since we want to analyze that part of the radio channel which is unaffected by noise, we will limit our search for propagation paths to that part of the APDP above a certain threshold P_{th}. First, we have to find a value for the noise floor P_{noise} itself, which we have calculated as being the median value of the APDP P_{Meas} between the time-delays $\tau_{n_0} = 200$ ns and $\tau_{max} = 341$ ns, which (after visual inspection) corresponded to those time-delays when all multipath components have been significantly attenuated, so that only the sum of all noise sources remains. After that, an extra margin of 3 dB was arbitrarily taken into account to significantly stay above the noisy part of the APDP, so that $P_{th}|_{\text{dB}} = P_{noise}|_{\text{dB}} + 3$ dB.

C. Propagation path detection

In this work, a propagation path is defined as a distinguishable peak at a certain delay bin in the APDP, assumed to be originating from a strong path between transmitter and receiver. It should be noted that, physically speaking, more than one propagation path could arrive in a certain delay bin. However, since the number of detected paths is not of importance for this work, but rather the power they represent, it makes no difference if this power originates from a single path or from multiple paths.

The method described here is a customized version of the one in [6], in which the search for propagation paths was done by finding the local maxima in the APDP. More particularly, a propagation path can be detected by comparing the power of the APDP P_{Meas} in each delay bin n with a threshold function $T(n)$, which can be defined mathematically as follows:

$$T(n) = \frac{\epsilon}{\Delta} \sum_{n-\frac{\Delta-1}{2}}^{n+\frac{\Delta-1}{2}} P_{Meas}(n). \qquad (4)$$

The function $T(n)$ calculates the local average value of the APDP in a region of Δ delay bins around each delay bin n, and adds an offset value ϵ of 3 dB in order to only detect those paths significantly above the local average in the APDP, and to disregard noise or strong diffuse multipath. As such, the propagation paths are then located in those bins n of the APDP which have a power greater than the threshold value $T(n)$. A path l can thus be defined by a value for the time-delay τ_l and

its corresponding power P_l in the APDP. Furthermore, τ_l is the time-delay of the n_l^{th} delay-bin, which is equal to $n_l \times \Delta\tau$. The path detection algorithm can be described as follows:

Algorithm 1: Detection of propagation paths

Input : P_{Meas}, $\Delta_{set} = \{17, 9, 5, 3\}$, $\texttt{paths}_{total} \leftarrow \{\varnothing\}$
Output: P_{SMC}, P_{DMC}

1 $P_{DMC} \leftarrow P_{Meas}$;
2 **foreach** $\Delta_i \in \Delta_{set}$ **do**
3 **repeat**
4 $\texttt{paths} \leftarrow \{\varnothing\}$;
5 **for** $n \leftarrow 1 + \frac{\Delta_i - 1}{2}$ ***to*** $M_f - \frac{\Delta_i - 1}{2}$ **do**
6 calculate $T(n)$ with $P_{DMC}(n)$ from Eq. (4) ;
7 **if** $P_{DMC}(n) > T(n)$ **then**
8 $\tau_l \leftarrow n \times \Delta\tau$; `// path delay`
9 $P_l \leftarrow P_{DMC}(n)$; `// path power`
10 $\texttt{paths} \leftarrow \texttt{paths} + \{\tau_l, P_l\}$;
11 $\texttt{paths}_{total} \leftarrow \texttt{paths}_{total} + \texttt{paths}$;
12 **for** $n \leftarrow 1$ ***to*** M_f **do**
13 calculate $P_{SMC}(n)$ with `paths` from Eq. (5) ;
14 $P_{DMC}(n) \leftarrow P_{DMC}(n) - P_{SMC}(n)$;
15 **foreach** *path* $l \in$ *paths* **do**
16 $P_{comp}(n_l) \leftarrow \frac{\Delta}{\epsilon} T(n_l) - P_l$;
17 $P_{DMC}(n_l) \leftarrow P_{DMC}(n_l) + P_{comp}(n_l)$;
18 **until** *paths is empty*;
19 **for** $n \leftarrow 1$ ***to*** M_f **do**
20 calculate $P_{SMC}(n)$ with $\texttt{paths}_{total}$ from Eq. (5) ;
21 **return** P_{SMC}, P_{DMC} ;

When a number of paths L has been detected (= size(`paths`)), we can construct an APDP originating from these L paths in the n^{th} delay bin as follows [6]:

$$P_{SMC}(n) = \sum_{l=1}^{L} P_l \left\{ \text{sinc}\left(\frac{\tau_n - \tau_l}{\Delta\tau} \right) \right\}^2, \qquad (5)$$

in which P_l and τ_l are the power and time-delay of a detected path l, respectively. Furthermore, τ_n is the time-delay of the n^{th} delay-bin, which is equal to $n \times \Delta\tau$.

Line 16 in Algorithm 1 calculates the average power around each delay bin n_l in the APDP based on the threshold function $T(n)$, from which we subtract the power of the detected peak P_l. This 'compensated' power $P_{comp}(n_l)$ is then added to $P_{DMC}(n_l)$ in line 17 to compensate for the removal of the detected peak P_l, and to get a power profile with a comparable power in n_l to its adjacent delay bins, in which no specular paths were detected.

As we can see from Algorithm 1, we will iterate over Δ values of 17, 9, 5, and 3 delay bins over which the threshold function $T(n)$ is calculated, corresponding with a spatial length of 1.6, 0.8, 0.4, and 0.2 m, respectively. This was done to ensure the detection of several closely spaced SMCs, of which their power could become merged throughout the time-delay domain, complicating their detection. The fact that we repeat the search for new paths for the same value of Δ was done in order to possibly detect new paths that were previously obscured by adjacent (stronger) paths.

It is straightforward to extend this algorithm for the detection of specular paths in each sub-band. We will take into account that specular paths should be found in the same delay bin over different sub-bands. However, the position of a peak in the APDP could be detected in an adjacent delay bin between e.g., the first and fourth sub-band due to spectral leakage. In order to overcome this issue, we took a margin of one time-delay bin into account when comparing the bins of the detected paths throughout the different sub-bands.

D. Diffuse spectrum modeling

The model for the diffuse spectrum $P_{DMC}(\tau)$ in Eq. (6) is based on the observation that the APDP has a base time-delay τ_d related to the distance between the transmitter and receiver, together with an exponential decay over time-delay caused by multiple reflections and scattering, indicated by a time constant τ_r, the reverberation time. Note that we compute a separate diffuse spectrum in each sub-band, after which we will compare the parameters describing them. Further discussion of this model can be found in [13] and [14].

$$P_{DMC}(\tau) = \begin{cases} \alpha_1 \, e^{\left(-\frac{\tau - \tau_d}{\tau_r}\right)} + \alpha_0, & \text{if } \tau > \tau_d \\ \alpha_0, & \text{otherwise.} \end{cases} \qquad (6)$$

In Eq. (6), α_1, τ_d, τ_r and α_0 are four parameters which fully describe the diffuse spectrum. The value for τ_d corresponds to the onset time (the base delay) of the diffuse spectrum P_{DMC}, and was taken as the delay bin corresponding with the strongest power in P_{DMC}, whilst the value for the Gaussian white noise α_0 was taken as the noise level of this spectrum, computed as the median value of P_{DMC} between the aforementioned time-delays $\tau_{n_0} = 200$ ns and $\tau_{max} = 341$ ns. The values for α_1 and τ_r were found after performing a linear regression of $P_{DMC}|_{\text{dB}}$ between τ_d and the time-delay when this diffuse power first dropped below the noise threshold $P_{noise}|_{\text{dB}}$ [15].

IV. Results

A. Power delay profiles

Fig. 3 presents an example of the measured APDP at 94 GHz for the processing of the 3 GHz bandwidth, and the remaining diffuse spectrum after removal of all detected specular components. It concerns an analysis of the 1st measurement position (denoted Tx-Rx link #1). In Fig. 3, the exponential DMC model fit according to Eq. (6) is shown in green.

Fig. 3 shows that all relevant specular propagation paths are reasonably well detected from the measured APDP by our path detection method. We can also state that the remaining diffuse spectrum has an exponential power decay over time-delay as proposed in Eq. (6), which corresponds to a linear power decay in a dB-scale, as depicted in Fig. 3.

Fig. 4 presents an example of the APDP at the same measurement position, but processed in sub-bands of 750 MHz.

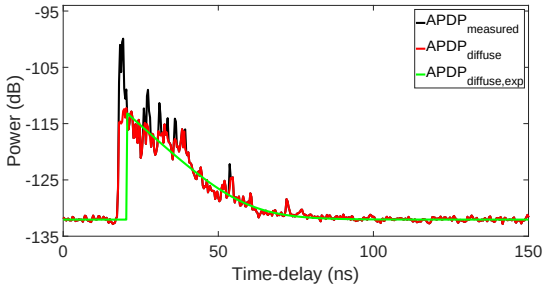

Figure 3: Measured APDP for Tx-Rx link #1 for the total frequency band (92.50 − 95.50 GHz), with the remaining diffuse spectrum after removal of all specular components, and the exponential fit of the diffuse spectrum.

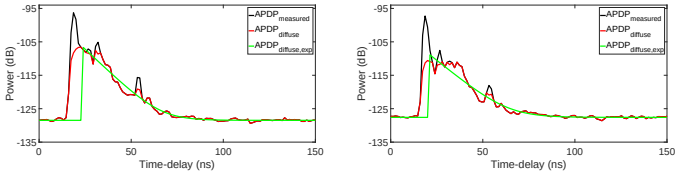

(a) sub-band A: 92.50-93.25 GHz **(b)** sub-band B: 93.25-94.00 GHz

(c) sub-band C: 94.00-94.75 GHz **(d)** sub-band D: 94.75-95.50 GHz

Figure 4: Measured APDP at 94 GHz in different frequency sub-bands, with the remaining diffuse spectrum after removal of all specular components, and the exponential fit of the diffuse spectrum for Tx-Rx link #1.

From Fig. 4, we can clearly see that the reduced bandwidth in the sub-bands causes a local spreading of the sampled frequency components. However, the overall shape of the diffuse spectrum in the sub-bands is very comparable to the one obtained after processing the 3 GHz band as a whole.

B. Specular power ratios

By comparing the power of the measured APDP P_{Meas} with the power attributable to specular propagation paths P_{SMC}, we can analyze how much power in the channel originates from these specular propagation paths, and how much can be attributed to diffuse powers. We therefore define p_r as the power ratio of the power in P_{SMC} and the measured power P_{Meas} as follows:

$$p_r = \frac{\sum_{n=1}^{Mf} P_{SMC}(n)}{\sum_{n=1}^{Mf} P_{Meas}(n)}. \tag{7}$$

Fig. 5 shows the power ratio p_r of the power P_{SMC} originating from the reconstruction of the detected propagation paths, and the total measured power P_{Meas} in the channel, both for the total measured 3 GHz band, as well as in the different sub-bands.

Fig. 5 shows that the detected path powers are similar for the total band and the various sub-bands. The small differences can be attributed to the difficult detection of paths throughout the sub-bands, as the reduced bandwidth (and hence larger

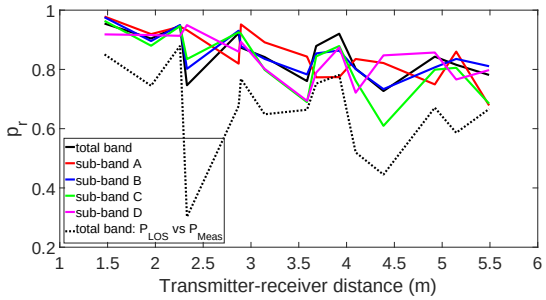

Figure 5: Ratio p_r of the power of the propagation paths P_{SMC} and the measured power P_{Meas}.

time-delay bin width) causes adjacent distinct paths to possibly become merged in a single delay bin. However, the detection of these delay bins will also result in the detection of their merged powers. This effect explains the minor differences between the results for the total band and the sub-bands.

Fig. 5 shows that the specular path powers dominate the diffuse powers for small Tx-Rx distances, representing 95 to 98% of the measured power. This effect becomes less noticeable at larger Tx-Rx distances over 5 m, where the SMC (and especially the line-of-sight (LOS) component) becomes less pronounced compared to the diffuse powers, and the power ratio p_r reduces from 95% to around 80%. The power of the LOS component compared to the measured power varies between 80% for the lower Tx-Rx distances to about 60% for the higher Tx-Rx distances. We have thus found that the power of the specular components at 94 GHz dominates those of the diffuse components, as they represent up to 80% and more of the total power in the channel. Hence, it becomes impossible to accurately model indoor radio channels at this frequency purely on the statistics of their diffuse components alone, which was an idea suggested in the original theory of room electromagnetics [7] at lower frequencies than in this work.

C. Path loss

We can approximate the path loss in the channel as follows:

$$PL = -10\log_{10}\left(\frac{1}{p_r}\sum_{l=1}^{L}\frac{P_l}{G_{TR}}\right), \tag{8}$$

in which the factor $\frac{1}{p_r}$ takes the proportion of power attributable to diffuse multipath components into account [16]. In addition, G_{TR} denotes the combined gain of transmit- and receive-antenna in our measurement scenario. It should be noted that the path loss according to this metric is influenced by the amount of specular paths estimated from the measurement data. However, we have noticed that the predominantly strongest propagation paths account for most of the path loss in the channel. Fig. 6 shows the resulting path loss according to Eq. (8).

From this measured path loss, we have constructed a path loss model L_f as follows:

$$L_f|_{\text{dB}} = L_{f,0}|_{\text{dB}} + 10\,n_f\,\log_{10}\left(\frac{d}{d_0}\right), \tag{9}$$

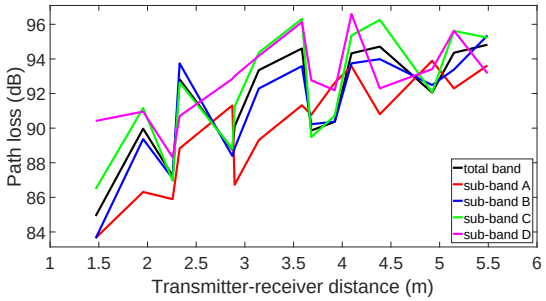

Figure 6: Measured path loss for different frequency bands. The black line represents the total 3 GHz band, the colored lines represent the path loss in each of the four sub-bands ranging from 92.50 GHz to 95.50 GHz.

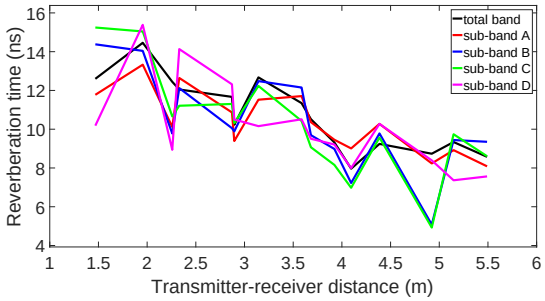

Figure 7: Reverberation time for the total 3 GHz bandwidth (black line), as well as in the different sub-bands (colored lines).

in which the intercept point $L_{f,0}$ is the path loss at an arbitrary reference distance d_0 (which was 1 m in our work) and for the frequency band denoted by f, and the variable n_f denotes the path loss exponent in this frequency band. All variables for this one-slope model were obtained by linear regression, and are summarized in Table II with the p-value of the n_f parameter. A p-value < 0.05 indicates that the null hypothesis can be rejected, meaning that the proposed one-slope model is a better fit than an intercept-only model, and that the coefficient n_f, regulating the influence of the Tx-Rx distance on the path loss, is a meaningful addition to the proposed model.

Table II: Overview of the one-slope path loss parameters.

frequency band	$L_{f,0}$ (dB)	n_f	F-statistic	p-value
total band	**84.27**	**1.40**	**17.96**	**0.0009679**
sub-band A	81.07	1.75	63.10	0.0000024
sub-band B	83.34	1.51	20.03	0.0006243
sub-band C	85.09	1.38	11.87	0.0043423
sub-band D	88.30	0.88	9.60	0.0084633

D. Diffuse spectrum

The reverberation time was estimated from the APDP by performing a regression analysis on the exponential power decay of the diffuse spectrum. This regression was performed in a dB-scale where this corresponds to a linear power decay. The regression was carried out between the mean power delay bin (the delay bin corresponding with the mean power value), and the noise delay bin [15]. By taking the mean power delay bin, we can reduce the influence of the strong line-of-sight components. These are typically present earlier on in the time-delay domain in the APDP, and might still be noticeable in the part that is regarded as the diffuse spectrum. Fig. 7 shows the reverberation time as a function of transmitter-receiver distance, both for the measured 3 GHz band, as well as in the different sub-bands.

Fig. 7 shows that the reverberation time is heavily dependent on the distance between transmitter and receiver. Decreasing reverberation times indicate that the electromagnetic waves spread themselves faster through a room for increasing Tx-Rx distances, increasing the power of the diffuse spectrum. This was validated by calculating the correlation coefficient between the Tx-Rx distances and the corresponding reverberation times, which was -0.88 for the total 3 GHz frequency band with a corresponding p-value of 1.2×10^{-5}. This work thus suggests that the theory of room electromagnetics is therefore not applicable at 94 GHz for this scenario, since the necessary condition of a rich scattering environment giving rise to a uniform distribution of power throughout a room, was clearly not met in our scenario. This is an important and interesting observation, as in contrast, scientific papers in lower frequency bands such as [14] or [15] found this theory to still be valid in the FCC-defined Ultra-Wideband (UWB) band. The UWB ranges from 3.1 GHz to 10.6 GHz, and might be the limit for the validity of the RE theory.

When performing a linear regression on the reverberation times as a function of transmitter-receiver distance d [m], we obtained that we can model it for the entire band by the function $\tau_r = a + b \times d$, for which the following values were obtained: $\tau_r = 15.38 - 1.33 \times d$ [ns], with an F-test statistic of 34.78 and a p-value of 5.3×10^{-5}. Performing the linear regression on the reverberation times again in the various sub-bands by shifting the measured results using the intercept point $a = 15.38$ ns of this model, we obtained the following frequency dependences b_f:

$$b_f = \begin{cases} -1.40 \ \frac{ns}{m}, & \text{sub-band A} \\ -1.46 \ \frac{ns}{m}, & \text{sub-band B} \\ -1.51 \ \frac{ns}{m}, & \text{sub-band C} \\ -1.48 \ \frac{ns}{m}, & \text{sub-band D.} \end{cases} \tag{10}$$

The corresponding F-test statistics with these linear regressions were all higher than 100 with p-values lower than 0.01, so we can state that the reverberation time decreases with transmitter-receiver distance d, and with increasing frequency.

E. RMS delay spread

In order to investigate how the detected propagation paths are spread out in time-delay, we look at the behavior of the root-mean-square (RMS) delay spread τ_{RMS}, which is a metric to define the multipath dispersion of a radio channel. This metric can be mathematically defined as follows:

$$\tau_{RMS} = \sqrt{\frac{\sum_n P(n)\ \tau_n^2}{\sum_n P(n)} - \left(\frac{\sum_n P(n)\ \tau_n}{\sum_n P(n)}\right)^2} \tag{11}$$

Fig. 8 shows the RMS delay spread for the total measured channel, as well as for the specular paths (SMC) and for

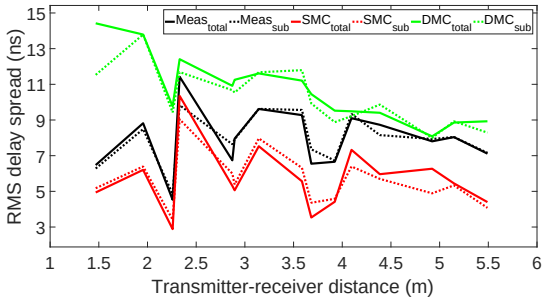

Figure 8: RMS delay spread of the measured channel, the specular part of the channel (SMC) and the diffuse part of the channel (DMC) for the total 3 GHz bandwidth, as well as in the different sub-bands.

the diffuse spectrum (DMC), both for the measured 3 GHz bandwidth, as well as in the different sub-bands.

Fig. 8 shows that the RMS delay spread of both the measured channel and the SMC seems to be nearly constant with distance, indicating that the detectable propagation paths do not become more spread out with Tx-Rx distance. This was supported by looking at the correlation coefficient, which was 0.03 with a p-value of 0.90 for the measured channel, and -0.11 with a p-value of 0.69 for the SMC. As we could see from Fig. 5, the power of the LOS component compared to the measured power varies between 80% for the lower Tx-Rx distances to about 60% for the higher Tx-Rx distances (with the exception of Tx-Rx #14). This explains why the RMS delay spread will be relatively constant as a function of Tx-Rx distance, since the LOS component is part of the SMC, and its dominant power will prevent other (reflected) paths from weighing in more on the RMS delay spread. For Tx-Rx #14, the relatively strong reflected paths form a more dispersive channel, resulting in a higher RMS delay spread. The fact that the measured channel shows the same behavior as the SMC can be supported by our previous claim that the measured channel (SMC+DMC) is dominated by the contribution of the SMC. No clear differences were found between the total 3 GHz band, and the (median) results in the different sub-bands.

The RMS delay spread of the diffuse part of the channel is higher than for the measured- or the specular part of the channel. The diffuse powers are more spread out in time-delay for shorter distances, and are less spread out with increasing distance. This was supported by looking at the correlation coefficient, which was -0.85 with a p-value of 0.000054. This fact can most likely be explained by looking at the measurement environment. When the Tx-Rx distance is low, the reflection arrive with relatively more power, making them easier to detect as specular paths, explaining why there is less DMC. When the Tx-Rx distance is high, the Tx is closer to the walls, resulting in the fact that the reflections at the receiver are closer to each other in the time-delay domain. This makes them harder to detect, resulting in more DMC. However, since these contributions lie very close to each other, this results in less delay spread.

F. Summary of measurement results

Table III summarizes our measurement results, conform with the parameters outlined in [6]. The results in this work can thus be used to generate channel models at 94 GHz in small indoor environments. It should be noted that the parameter $P_d|_{\text{dB}}$ in this work corresponds to $(\alpha_1 + \alpha_0)|_{\text{dB}}$ in [6], and that β_d is simply the reverberation time τ_r. The parameters P_0 and β_0 correspond with the initial path loss and a power decay factor, respectively and σ_s is the standard deviation of the shadow fading. All these parameters are maximum likelihood estimates of the log-likelihood function (12) in [6].

Table III: Overview of the measurement results for the 92.50−95.50 GHz band.

	P_d (dB)	β_d (ns)	P_0 (dB)	β_0 (ns)	σ_s (dB)	
Tx-Rx #15 (1.47 m)	-116.71	12.60	12.60	8.46	6.12	
Tx-Rx #11 (1.96 m)	-114.33	14.46	14.46	10.41	5.02	
Tx-Rx #12 (2.26 m)	-113.69	12.45	12.45	24.08	5.76	
Tx-Rx #14 (2.33 m)	-113.16	12.05	12.05	9.00	3.23	
Tx-Rx #13 (2.87 m)	-113.99	11.67	11.67	9.22	4.87	
Tx-Rx #10 (2.90 m)	-113.81	10.23	10.23	14.13	4.96	
Tx-Rx #8 (3.14 m)	-114.50	12.67	12.67	7.98	3.95	
Tx-Rx #9 (3.59 m)	-115.47	11.34	11.34	13.89	4.33	
Tx-Rx #7 (3.68 m)	-112.82	10.52	10.52	10.71	4.46	
Tx-Rx #4 (3.92 m)	-115.64	9.32	9.32	12.47	5.35	
Tx-Rx #5 (4.10 m)	-114.72	7.96	7.96	13.84	3.32	
Tx-Rx #6 (4.39 m)	-116.47	9.24	9.24	7.15	3.87	
Tx-Rx #3 (4.92 m)	-117.50	8.74	8.74	10.98	4.39	
Tx-Rx #2 (5.15 m)	-115.78	9.34	9.34	20.21	3.77	
Tx-Rx #1 (5.49 m)	-112.82	8.57	8.57	8.75	2.83	

V. Conclusions

This work presents a method which enables the estimation of specular propagation paths from Multiple-Input Multiple-Output measurement data, for different frequency sub-bands. It separates the data into specular and dense multipath components (SMC and DMC). This method was applied in an indoor environment at 94 GHz by performing a frequency-domain channel sounding procedure with virtual arrays. We investigated the path loss, root-mean-square delay spreads and SMC ratios for the different sub-bands as a function of transmitter-receiver distance. Based on the diffuse spectrum, the behavior of the reverberation time was found to be heavily

dependent on transmitter-receiver distance, indicating that the necessary condition of a rich scattering environment was not met, therefore disproving the theory of room electromagnetics at 94 GHz for this environment. This was also proven by looking at the relative power of the specular components, as they represent up to 80% and more of the total power in the channel.

Future work consists of performing an extensive full polarimetric measurement campaign at 94 GHz in Line-of-Sight (LoS), Obstructed-LoS and Non-LoS environments, and the analysis of SMC and DMC parameters in these scenarios.

ACKNOWLEDGMENT

Brecht Hanssens is funded by a Ph.D. grant of the Agency for Innovation by Science and Technology (IWT). Emmeric Tanghe is a Post-Doctoral Fellow of the Research Foundation Flanders (FWO). This work was carried out in the framework of COST Action CA15104 IRACON, and was supported by the FWO project G027714N, IAP BESTCOM, as well as the Ministerio de Economía y Competitividad MINECO, Spain (TEC2013-47360-C3-2-P) and by the European FEDER funds.

REFERENCES

[1] S. Bakhtiari, N. Gopalsami, T. W. Elmer, et al. Millimeter Wave Sensor for Far-Field Standoff Vibrometry, 2014. US Patent 8,686,362.

[2] J. W. May and G. M. Rebeiz. Design and Characterization of W -Band SiGe RFICs for Passive Millimeter-Wave Imaging. *IEEE Transactions on Microwave Theory and Techniques*, 58(5):1420–1430, 2010.

[3] A. Kajiwara. Indoor Propagation Measurements at 94 GHz. In *IEEE International Symposium on Personal, Indoor and Mobile Radio Communications. Wireless: Merging onto the Information Superhighway*, volume 3, pages 1026–1030, 1995.

[4] J. Helminger, J. Detlefsen, and H. Groll. Propagation Properties of an Indoor-Channel at 94 GHz. In *International Conference on Microwave and Millimeter Wave Technology Proceedings*, pages 9–14, 1998.

[5] R. Piesiewicz, R. Geise, M. Jacob, et al. Indoor Channel Measurements of Point-to-Point Ultra Broadband Short Range Links Between 75 GHz and 110 GHz. In *Antennas and Propagation Society International Symposium*, pages 1–4, 2008.

[6] K. Haneda, J. Järveläinen, A. Karttunen, et al. A Statistical Spatio-Temporal Radio Channel Model for Large Indoor Environments at 60 and 70 GHz. *IEEE Transactions on Antennas and Propagation*, 63(6):2694–2704, 2015.

[7] J. B. Andersen, J. O. Nielsen, G. F. Pedersen, et al. Room Electromagnetics. *IEEE Antennas and Propagation Magazine*, 49(2):27–33, 2007.

[8] M.-T. Martínez-Inglés, J.-M. Molina-García-Pardo, D. P. Gaillot, et al. Polarimetric Indoor Measurements At 94 GHz. In *European Conference on Antennas and Propagation*, pages 1–3, 2016.

[9] B. Hanssens, M-T Martínez-Inglés, E. Tanghe, et al. Measurement-based Analysis of Reverberation Times At 94 GHz in an Indoor Environment. In *European Conference on Antennas and Propagation*, 2017.

[10] Federal Communications Commission (FCC). First report and order 02-48, 2002.

[11] M.-T. Martínez-Inglés, D. P. Gaillot, J. Pascual-Garcia, et al. Channel sounding and indoor radio channel characteristics in the w-band. *EURASIP Journal on Wireless Communications and Networking*, (1):1–8, 2016.

[12] L. Bernadó. *Non-Stationarity in Vehicular Wireless Channels*. PhD thesis, Institut für Nachrichtentechnik und Hochfrequenztechnik, Technische Universität Wien, Vienna, Austria, 2012.

[13] A. Richter. *Estimation of Radio Channel Parameters: Models and Algorithms*. PhD thesis, Technische Universität Ilmenau, Fakultät für Elektrotechnik und Informationstechnik, Ilmenau, Germany, 2005.

[14] A. Bamba, M. T. Martínez-Inglés, D. P. Gaillot, et al. Experimental Investigation of Electromagnetic Reverberation Characteristics as a Function of UWB Frequencies. *IEEE Antennas and Wireless Propagation Letters*, 14:859–862, 2015.

[15] B. Hanssens, M.-T. Martínez-Inglés, A. Bamba, et al. Estimation of Room Electromagnetics Reverberation Time for Ultra-Wideband Indoor Channels. In *European Conference on Antennas and Propagation*, pages 527–528, 2014.

[16] K. Haneda, S. L. H. Nguyen, J. Järveläinen, et al. Estimating the Omni-Directional Pathloss From Directional Channel Sounding. In *European Conference on Antennas and Propagation*, pages 1–5, 2016.